Experimental and numerical study of the low temperature behaviour of $LiYbF_4$

Aurore Finco[1, 2]

[1] *Laboratory for Quantum Magnetism, École Polytechnique Fédérale de Lausanne (EPFL)*
[2] *ICFP, Département de physique, École normale supérieure*

(Dated: August 9, 2013)

$LiYbF_4$ is a quantum antiferromagnet, with $T_N = 128$ mK, in which the magnetic moments are coupled through dipolar interactions and present a strong planar anisotropy. The magnetic moments have the same characteristics in $LiErF_4$, which was established as a model whose thermal phase transition belongs to the XY/h4 two-dimensional universality class[1]. Both $LiErF_4$ and $LiYbF_4$ exhibit a quantum phase transition when a DC field is applied along the crystallographic c-axis, with $H_c = 4$ kOe and 4.8 kOe respectively. The numerical part of this study consists in further work on a code for classical Monte Carlo simulations based on a classical effective model derived from the quantum model, in order to compute thermodynamical quantities and critical exponents. This Monte Carlo code can then be further expanded to study disordered compounds such as $LiHo_{1-x}Er_xF_4$ and $LiHo_{1-x}Yb_xF_4$. Related to this, an experimental protocol was developed to determine the composition of these samples using measurements of their magnetic moments. On the experimental side, this work represents the first comprehensive study of the low-temperature properties of $LiYbF_4$. The H-T phase diagram of $LiYbF_4$ has been mapped out using AC susceptibility measurements of single crystals in a dilution refrigerator.

I. INTRODUCTION

The $LiREF_4$ (where RE is for rare earth) compounds are anisotropic dipolar coupled magnetic systems in which the long-range dipolar interaction between the magnetic moments of the rare earth ions dominates the short-range exchange interaction. Luttinger and Tisza published in 1946[2] a theoretical discussion about the emergence of a long range order in this kind of systems and found that both ferromagnetic and antiferromagnetic order can appear.

The $LiREF_4$ systems are therefore used to study theoretical microscopic models : the Hamiltonian describing the systems is quantitatively known, and thus numerical predictions can be compared to experimental data. Depending on the rare earth ion considered, ferromagnetic (with Ho for instance) and antiferromagnetic (with Er or Yb) behaviour are observed at low temperature. The $LiREF_4$ systems can also be diluted with non magnetic Y or be a mixture of several types of ions. Thus disordered systems like $LiHo_{1-x}Er_xF_4$ or $LiHo_{1-x}Yb_xF_4$ in which a spin glass phase was observed[3] can be obtained.

Here, the low temperature behaviour of $LiYbF_4$ is investigated by AC susceptibility measurements to map out the H-T phase diagram, mean field and Monte Carlo simulations. $LiYbF_4$ is an antiferromagnet which possesses the same type of planar anisotropy in the xy plane as $LiErF_4$. The interest in $LiYbF_4$ is that the crystal field provides a larger planar anisotropy than in $LiErF_4$, which should therefore be a cleaner model dipolar-coupled XY antiferromagnet. In these two compounds, two types of phase transitions are observed: the usual thermal phase transition, driven by the thermal fluctuations, and a quantum phase transition, which is a transition occurring at $T = 0$ K when a transverse magnetic field is applied.

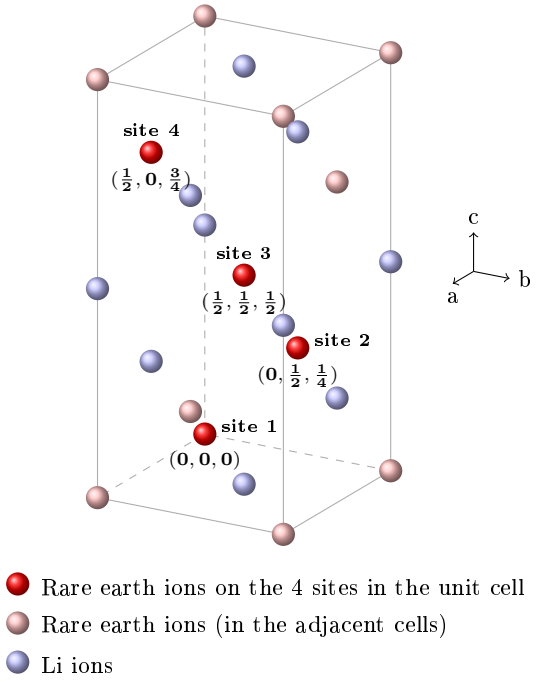

Figure 1: Schema of a unit cell of $LiREF_4$. For clarity reasons, the fluoride ions are not represented.

II. DESCRIPTION OF THE SYSTEM

A. The $LiREF_4$ structure

The crystalline structure of $LiREF_4$ is tetragonal and belongs to the space group $I4_1/a$, the n°88 in the International Tables for Cristallography[4] (Scheelite structure). The magnetic moments are carried by the rare earth ions, whose positions in the unit cell are shown in figure 1. The unit cell contains 4 rare earth ions.

Table I: Quantum numbers and lattice parameters[5] for the different rare earth ions considered.

	Yb	Er	Ho
L (orbital momentum)	3	6	6
S (spin momentum)	1/2	3/2	2
J (total momentum)	7/2	15/2	8
g (Landé factor)	8/7	6/5	5/4
μ_{eff} (μ_B)	4.5	9.6	10.6
Lattice constant a (Å)	5.132	5.162	5.175
Lattice constant c (Å)	10.59	10.70	10.75

In the following, different rare earth ions will be considered: mostly Yb ($Z = 70$), but also Er ($Z = 68$) and Ho ($Z = 67$). Their electronic configuration are respectively $4f^{14}$,$4f^{12}$ and $4f^{11}$. These ions have different quantum numbers for the orbital momentum, leading to different values of their magnetic moment: an effective magnetic moment can be defined as $\mu_{\text{eff}} = g\ \mu_B\ \sqrt{J(J+1)}$, where g is the Landé factor, $\mu_B \simeq 5.78 \cdot 10^{-2}$ meV/T the Bohr magneton and J the total momentum quantum number. Er and Ho have both large moments and their values are close while the moment of Yb is twice as small. The useful parameters are regrouped in the table I.

B. Single-ion Hamiltonian

The Hamiltonian can be separated in two parts, single-ion and interactions with neighbouring ions. The single-ion part can itself be separated in several contributions: the crystal field, the Zeeman Hamiltonian and the hyperfine coupling.

$$\mathcal{H} = \mathcal{H}_{\text{cf}} + \mathcal{H}_{\text{Z}} + \mathcal{H}_{\text{hyp}} + \mathcal{H}_{\text{int}} \tag{1}$$

1. *The crystal field*

The main contribution to the single-ion Hamiltonian is the crystal field, which is due to the electric field induced by the charge distribution in the lattice and which creates the magnetic anisotropy by acting on the $4f$ electrons. A convenient way to express the Hamiltonian $\mathcal{H}_{\text{cf}}$ is to use the Stevens operators (which are defined in Appendix A).

$$\mathcal{H}_{\text{cf}} = \sum_i \sum_{lm} B_l^m \hat{O}_l^m(\vec{J}_i) \tag{2}$$

The parameters for each rare earth ion were measured using neutron scattering. For Yb, Er and Ho, the crystal field parameters are given in the table X. The dominant part of the crystal fields of $LiHoF_4$ and of $LiErF_4$ and $LiYbF_4$ have opposite signs, leading to different anisotropies, and thus to completely different behaviours. This term is $\propto J_z^2$, with a negative factor for $LiHoF_4$ which makes ferromagnetic order energetically favourable. Thus $LiHoF_4$ is a model magnet for the Ising model in a transverse field — at low temperature the Ho moments align in the direction of the c-axis, leading to a ferromagnetic long range order. In $LiErF_4$ and $LiYbF_4$, the factor is positive and the moments are preferentially in the ab plane and interact antiferromagnetically, forming at low temperature a bi-layered antiferromagnetic (BLAFM) structure. This structure presents a rotational symmetry in the ab plane. It can indeed be shown that the dipolar coupling is invariant under a rotation of the magnetic moments in each layer of an angle $(-1)^l\theta$ around the c-axis, where l is the layer index. Nevertheless, this transformation does not leave invariant the crystal field, which retains only a four-fold rotational symmetry around the c-axis. Consequently the two equivalent orderings are shown on the figure 2. In $LiYbF_4$, $LiErF_4$ and $LiHoF_4$, the ground state of $\mathcal{H}_{\text{cf}}$ is doubly degenerate and the first excited state has a much higher energy. The gap between the ground-state and the first excited state for $LiYbF_4$ is 334.8 K, 11.5 K for $LiHoF_4$ and 25.7 K for $LiErF_4$. Hence, at low temperature, the excited states of the crystal field will not be considered. The table X gives two sets of parameters for the crystal field in $LiYbF_4$. Indeed, all the computations were done with the first set and the result for the critical field was 50 times larger than the measured value. Finally, by fitting the neutron scattering data[20] and the susceptibility data from those work, a new set of parameters was found, which gives, in mean field, a value of the critical field which corresponds to the experimental value. The mean field calculations were performed again with these new parameters but the Monte Carlo simulation was too slow to be run again. Interestingly, the new values for the parameters are close from the previous one, they actually are within the error bar but they lead to a totally different behaviour at 0 K, for the quantum phase transition.

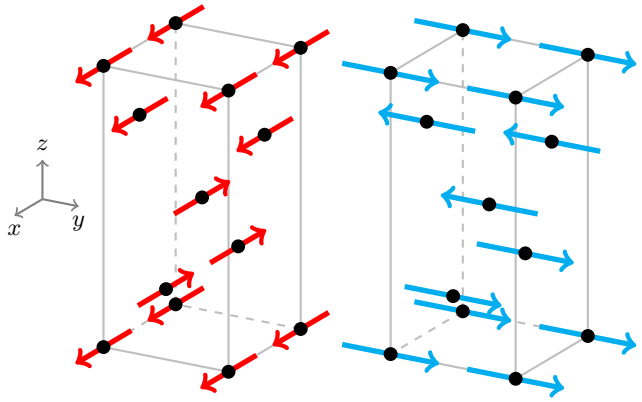

Figure 2: Schema of the Bi-Layered AntiFerroMagnetic (BLAFM) ordered structure in $LiErF_4$ and $LiYbF_4$. On the left picture, the moments are aligned parallel to the x axis, on the right they are aligned parallel to the y axis. There is a rotational symmetry in the xy plane but each layer rotates in a different way as its neighbours.

2. The Zeeman term

Another part of the single-ion Hamiltonian is the Zeeman term, the coupling of the moments with the external magnetic field. Thus, the Zeeman Hamiltonian is written as :

$$\mathcal{H}_{\rm Z} = -\mu_B \; g_L \vec{J}.\vec{B}, \tag{3}$$

where g_L is the Landé factor which depends on the electronic configuration of the ion, $\vec{J}$ represents the total momentum operator and $\vec{B}$ is the external field. The effect of the Zeeman interaction is to align the magnetic moments in the direction of the external field.

3. The hyperfine coupling

The last part of the single-ion Hamiltonian is the hyperfine coupling, which is the coupling between the electronic magnetic moment and the nuclear spin. For an isotropic interaction, the corresponding Hamiltonian is given as:

$$\mathcal{H}_{\rm hyp} = A \; \vec{J} \cdot \vec{I}, \tag{4}$$

where $\vec{I}$ is the nuclear spin operator and A is the coupling constant. For Ho, the only stable isotope (^{165}Ho) possesses a nuclear spin of 7/2 and $A_{\rm Ho} = 3.36$ μeV[6].
Er has 6 stable isotopes but only one of them, ^{167}Er, possesses a non-zero nuclear spin of 7/2. Its natural abundance is 22.8% and $A_{\rm Er} = 0.43$ μeV[7].
There are 7 stable isotopes of Yb, and two of them carry a nuclear moment: ^{171}Yb, whose quantum number is 1/2 and whose natural abundance is 14.3%, and ^{173}Yb, whose quantum number is 5/2 and whose natural abundance is 16.2%[8]. The coupling constants have the following values: $A^{171}_{\rm Yb} = 11.0$ μeV and $A^{173}_{\rm Yb} = -3.0$ μeV[9].

C. Interaction Hamiltonian

1. Exchange interaction

The exchange interaction is a short-range pair interaction between magnetic moments, whose Hamiltonian is given by:

$$\mathcal{H}_{\rm ex} = \sum_{\substack{i,j \\ (n.n.)}} \mathcal{J}_{ij} \; \vec{J}_i \cdot \vec{J}_j \tag{5}$$

where the sites i and j are nearest neighbours. In $LiREF_4$, the $4f$ electrons are tightly bound to the rare earth ions and thus the exchange interaction will be negligible compared to the dipolar interaction. This interaction will therefore not be considered in the following.

2. Dipolar interaction

For the materials considered herein, the dominant interaction between the moments is the dipolar interaction, which leads to antiferromagnetic order in $LiYbF_4$ and $LiErF_4$ and to ferromagnetic order in $LiHoF_4$. The dipolar interactions are long-range pair interactions, therefore all the pairs of moments in the lattice should be taken into account in $\mathcal{H}_{\rm dip}$:

$$\mathcal{H}_{\rm dip} = -\frac{1}{2} \sum_{i,j} g_{L_i} \; g_{L_j} \; \mu_B^2 \; \vec{J}_i D_{ij} \vec{J}_j \tag{6}$$

where D_{ij} is the matrix for the dipole-dipole interaction between sites i and j. D_{ij} can be derived from the classical dipole-dipole interaction:

$$D_{ij} = \frac{\mu_0}{4\pi} \left(\frac{3 \; r_{ij} r_{ij}^{\rm T}}{||r_{ij}||^5} - \frac{\delta_{ij}}{||r_{ij}||^3} \right) \tag{7}$$

Finally, the total Hamiltonian of the system is the sum of the single-ion Hamiltonian and of the interaction Hamiltonian (which is reduced to the dipolar interactions because the exchange interaction is neglected).

III. NUMERICAL SIMULATION

A. Mean-field computation

A first approach to simulate the system and to take into account the interactions between the ions is the mean-field approximation. In this approximation, the fluctuations of the moments around their equilibrium position is neglected. In the mean-field approximation, J_i is replaced in $\mathcal{H}_{\rm dip}$ (6) by $(J_i - \langle J_i \rangle) + \langle J_i \rangle$, where $(J_i - \langle J_i \rangle)$ is the fluctuation term and is considered small. Then, the second order terms are neglected and the constant is removed. Since $D_{ij} = D_{ji}$ and D_{ij} is symmetric,

$$\mathcal{H}^{\rm MF}_{\rm dip} = -\sum_{i,j} g_{L_i} \; g_{L_j} \; \mu_B^2 \; \vec{J}_i D_{ij} \langle \vec{J}_j \rangle. \tag{8}$$

An effective mean-field can be introduced; $\vec{h}^i_{\rm eff} = \sum_{j=1}^{4} \tilde{D}_{ij} \langle \mu_B g_{L_j} \vec{J}_j \rangle$, where the i index varies from 1 to 4, for the 4 sites in the unit cell. The $\tilde{D_{ij}}$ matrices are defined by:

$$\tilde{D}_{ij} = \frac{N}{V} \left(\frac{4\pi}{3} + \sum_{\rm cells} D_{ij} - \mathcal{N}_{ij} \right). \tag{9}$$

The first term is the Lorentz factor[10], the second one the sum of the D_{ij} matrices over a large number of unit cells inside a sphere of radius 100 cells, and the third one is

the demagnetization factor (see Appendix C). This can be shown to be equivalent to

$$\mathcal{H}_{\rm dip}^{\rm MF} = \sum_{i=1}^{4} g_{L_i}\ \mu_B\ \vec{J}_i \cdot \vec{h}_{\rm eff}^{\,i}, \tag{10}$$

in which all sites are decoupled. Once this Hamiltonian is established, the calculation (which computes the values only in one unit cell) is as follows:

- The matrices $\tilde{D}_{ij}$ are computed once at the beginning.
- The moments $\langle J_i \rangle$ are initialized in a given arbitrary configuration.
- The mean fields $\vec{h}_{\rm eff}^{\,i}$ are computed from the current configuration of the moments.
- The mean field hamiltonians for each sites $\mathcal{H}_i^{\rm MF} = \mathcal{H}_{\rm cf}^i + \mathcal{H}_{\rm Z}^i + \mathcal{H}_{\rm hyp}^i + \mathcal{H}_{\rm dip}^{i\ \rm MF}$ are diagonalized and the means moments $\langle J_i \rangle$ are updated.
- The difference $\Delta = \sum_i |\langle J_i \rangle^{new} - \langle J_i \rangle^{old}|$ is evaluated and compared to a convergence threshold $\varepsilon = 10^{-6}$. If $\Delta > \varepsilon$, the algorithm returns to the third step, if $\Delta < \varepsilon$, it returns the values of $\langle J_i \rangle$.

Since the fluctuations are neglected, the critical temperature will be overestimated. Furthermore, as the fluctuations increase at the transition, the behaviour of the system around the transition (and hence the critical exponents) can not be accurately described by this mean field approximation. However, these mean field simulations provide a basis for comparison with the results of the Monte Carlo simulations and the experimental data.

B. Monte Carlo simulation

1. The effective model

a. A quantum spin 1/2 effective model In the Monte Carlo simulation, the considered Hamiltonian is $\mathcal{H} = \mathcal{H}_{\rm cf} + \mathcal{H}_{\rm Z} + \mathcal{H}_{\rm dip}$. The dipolar interactions will be treated classically. The first step to derive the effective model is then to find a simple model for the single ion Hamiltonian $\mathcal{H}_0 = \mathcal{H}_{\rm cf} + \mathcal{H}_{\rm Z}$. Since only the low temperature behaviour will be studied here, the excited states of the crystal field will almost never be reached by the system, which will stay in the two lowest energy states. The degeneracy is lifted when the external field is applied, the doublet is split in two states with different energies. This observation leads to a simplified model for the single ion Hamiltonian, an effective spin 1/2 model. To construct this model, the J operators and the single ion Hamiltonian are projected on the subspace generated by the two low energy states $|1\rangle$ and $|2\rangle$. Four matrices of size 2×2, $\tilde{J}_x$, $\tilde{J}_y$, $\tilde{J}_z$ and $\tilde{\mathcal{H}}_0$ are obtained. The Ising basis

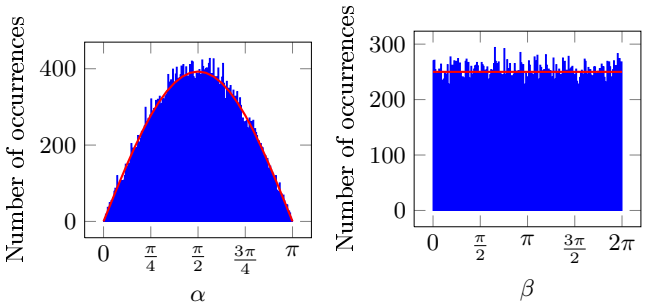

(a) Distribution of α (b) Distribution of β

Figure 3: Distributions $\rho_\alpha {\rm d}\alpha$ and $\rho_\beta {\rm d}\beta$ over $5\cdot10^4$ calls of the function with ${\rm d}\alpha = {\rm d}\beta = \frac{\pi}{100}$. The red lines are the theoretical distributions.

$\{|+\rangle, |-\rangle\}$ will be the eigenbasis of $\tilde{J}_z$ in which the others operators are then computed. With this technique, the dimension of the Hilbert space is reduced from $2J+1$ (ie 8 for Yb, 16 for Er and 17 for Ho) to 2. The states of this Hilbert space will be expressed in terms of the angles defining the quantum state on the Bloch sphere:

$$|\alpha, \beta\rangle = \cos(\alpha)\,|+\rangle + e^{{\rm i}\beta}\sin(\alpha)\,|-\rangle \tag{11}$$

where $\alpha \in [0, \frac{\pi}{2}]$ and $\beta \in [0, 2\pi]$.

b. The classical effective model In the quantum model, there are two degrees of freedom, the angles α and β. In a classical model, for a moment whose position is fixed at the position of the ion in the unit cell, there are also two degrees of freedom to determine the orientation of the moment. Thus, the effective classical moment will be defined by the two angles α and β which will be stored (and so will be the moment value) for each site of the lattice. Then for these values of α and β and of the external field, the mean value of the $\tilde{J}$ operators and of $\tilde{\mathcal{H}}_0$ in the state $|\alpha, \beta\rangle$ is evaluated and the classical moment is defined as the mean value of $\tilde{J}$ in this state. In order to perform the Monte Carlo simulation, it is also necessary to find a way to change randomly the direction of the moments. This is done by drawing randomly the two angles α and β, with a distribution such as the states $|\alpha, \beta\rangle$ are uniformly distributed on the north hemisphere of the Bloch sphere (see section III B 1 c). In terms of probability distributions,

$$\rho_\beta(\beta) = \frac{1}{2\pi},\ \beta \in [0, 2\pi]$$
$$\rho_\alpha(\alpha) = \frac{\sin(\alpha)}{2},\ \alpha \in [0, \pi]$$

To pick uniformly a random vector on the unit sphere, the Marsaglia method is employed[11]. Figure 3 shows a test of the function which gives α and β, during which $5\cdot10^4$ random pairs (α, β) were generated. The distributions correspond to those expected.

c. Distribution of the moments, anisotropy The anisotropy in the xy plane for $LiYbF_4$ and $LiErF_4$ and

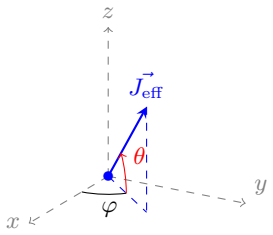

Figure 4: Definition of the angles θ and φ for the effective moment.

along the z axis in $LiHoF_4$ comes from the values of the crystal field parameters and should therefore appear in the classical effective model. The orientation of the moment is determined by two angles θ and φ which are defined on the figure 4. More precisely, the definitions of θ and φ are the following:

$$\tan(\theta) = \frac{\langle \alpha, \beta | \tilde{J}_z | \alpha, \beta \rangle}{\sqrt{\left(\langle \alpha, \beta | \tilde{J}_x | \alpha, \beta \rangle\right)^2 + \left(\langle \alpha, \beta | \tilde{J}_y | \alpha, \beta \rangle\right)^2}} \tag{12}$$

$$\tan(\varphi) = \frac{\langle \alpha, \beta | \tilde{J}_y | \alpha, \beta \rangle}{\langle \alpha, \beta | \tilde{J}_x | \alpha, \beta \rangle} \tag{13}$$

When α and β vary, the evolution of θ and φ leads to several observations. First, a change of α only changes θ and a change of β modifies only φ. Then, the distribution of φ is uniform when the distribution of β is uniform: the symmetry under rotation in the xy plane is respected. The anisotropy appears in the θ distribution. A first remark is that when $\alpha \in [0, \pi]$, the direction $+z$ is favoured, a magnetization in this direction appears at high temperature. This magnetization is certainly not physical, it was still observed at 50 K and there is no reason to prefer $+z$ to $-z$. The explanation for this behaviour is shown in figure 5. Since $\rho_\alpha = \sin(\alpha)/2$, the cases where α is near 0 or π are less frequent than those where α is around $\frac{\pi}{2}$. In addition, $\alpha = \frac{\pi}{2}$ leads to $\theta = \frac{\pi}{2}$, ie $\vec{J_{\text{eff}}}$ along $+z$ whereas $-z$ corresponds to $\alpha = 0$ or π. This explains the preference of the magnetization along $+z$ which is removed when α is fixed between 0 and $\frac{\pi}{2}$. The anisotropy is clearly visible in figure 5, especially for $LiYbF_4$ and $LiHoF_4$. For $LiYbF_4$, the probability distribution is sharply peaked at $\theta = 0$, therefore the moments are confined in the xy plane. For $LiHoF_4$, $\theta \simeq \pm\frac{\pi}{2}$ for most of the values of α, the moments remain aligned in the z direction. In $LiErF_4$, the anisotropy is less pronounced but marked by the inflexion point at $\theta = 0$.
The combination of the α and β distributions with the curves of θ for each ion leads to the distributions of θ of the figure 5, showing again clearly the anisotropy. The graphs were plotted with 5.10^4 randomly drawn pairs (α, β). Furthermore, the anisotropy appears also in the norm of the moments, which depends on their direction. When α and β vary continuously, the moment describes

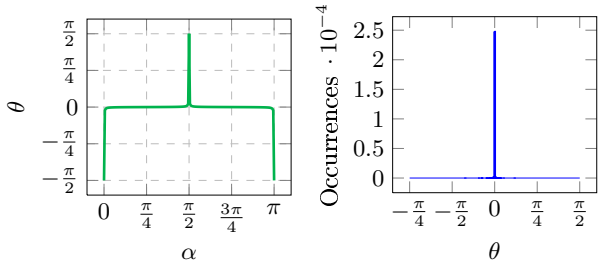

(a) $LiYbF_4$, old parameters

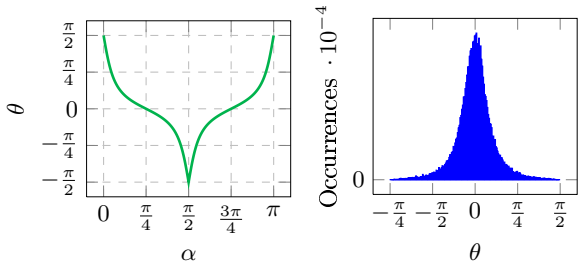

(b) $LiYbF_4$, new parameters

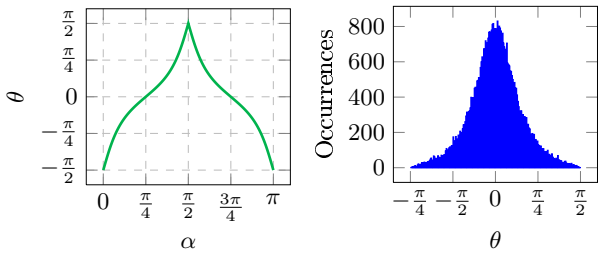

(c) $LiErF_4$

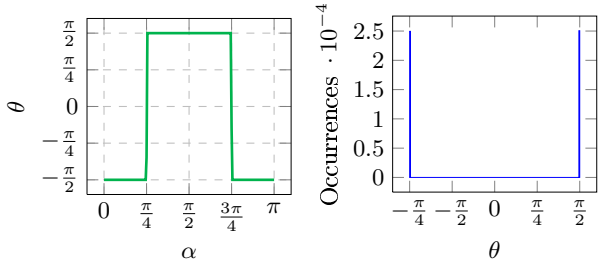

(d) $LiHoF_4$

Figure 5: θ as a function of α (with β fixed to 0) and distributions of θ in $LiYbF_4$, $LiErF_4$ and $LiHoF_4$.

an ellipsoid, as shown in figure 6. These ellipsoids show also clearly the anisotropy induced by the crystal field. The figures 5 and 6 show the distributions and the ellipsoids obtained from the two sets of crystal field parameters for $LiYbF_4$. The anisotropy was excessive with the first set of parameters, which explains why the critical

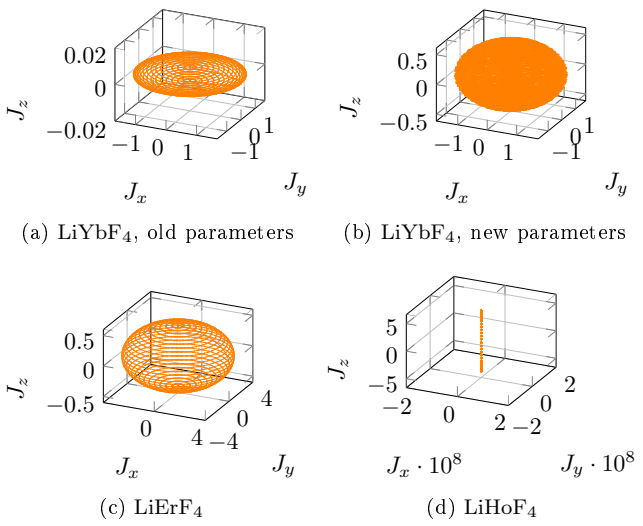

(a) $LiYbF_4$, old parameters (b) $LiYbF_4$, new parameters

(c) $LiErF_4$ (d) $LiHoF_4$

Figure 6: Ellipsoids described by $\vec{J_{\text{eff}}}$ when α varies in $[0, \frac{\pi}{2}]$ and β in $[0, 2\pi]$.

field was so much overestimated. The new set of parameters should give a more reasonable value for H_C.
In this classical effective model, the number of degrees of freedom (the two angles) is the same as in the quantum effective spin 1/2 model, and the anisotropy comes from both the norm of the moments, which depends on their direction, and from the probability distribution of the directions when they are randomly drawn in the Monte Carlo algorithm.

2. *The Monte Carlo algorithm*

Once the effective model is established, the aim is to simulate the whole system. A lattice is build in a cubic box of L unit cells in each direction. The lattice is populated with given proportions of Yb, Er and Ho, randomly placed. The same method as in the mean-field is used to compute the dipolar interaction matrices and the interaction energy is computed with the classical moments.
The system evolves according to the following algorithm: an ion is randomly picked. A couple of angles α and β are also randomly drawn. The effective moment corresponding to the chosen ion and the new angles is computed. The energy variation $\mathrm{d}\mathcal{E}$ between the previous configuration and the new one (with the rotated moment) is calculated. The Metropolis criterion is then used to decide if the rotation of the moment is kept or not:

- if $T = 0$ K, the rotation is accepted only if $\mathrm{d}\mathcal{E} < 0$.
- if $T > 0$ K, if $\mathrm{d}\mathcal{E} < 0$, the rotation is accepted and if $\mathrm{d}\mathcal{E} > 0$, it is accepted with the probability $e^{-\mathrm{d}\mathcal{E}/k_B T}$.

This process is iterated during $N_{\text{eq}} = 2 \cdot 10^6$ steps in order to reach equilibrium (see Appendix B). Once the system is in equilibrium, the measurement is performed during $N_{\text{meas}} = 10^6$ iterations. The magnetization and the energy are measured every N_{ions} (the number of ions in the system) iterations. This way, the algorithm picks roughly every ion between two measurements. The values are averaged over a large number of steps. In $LiYbF_4$ and $LiErF_4$, the order parameter is the staggered magnetization in the xy plane. The staggered magnetization in the x and y directions J_x^{alt} and J_y^{alt} are computed by adding the x or y components of the four moments in the unit cell with alternated signs:

$$J_x^{\text{alt}} = J_x^1 - J_x^2 - J_x^3 + J_x^4$$
$$J_y^{\text{alt}} = J_y^1 + J_y^2 - J_y^3 - J_y^4$$

and the order parameter J_{xy}^{alt} is defined by:

$$J_{xy}^{\text{alt}} = \sqrt{(J_x^{\text{alt}})^2 + (J_y^{\text{alt}})^2}$$

In order to have accurate values for the critical exponents, the field and temperature scans are averaged over a large number of realizations (around 100 measurements with circa 10 different equilibrium configurations).

3. *Results*

Using the classical effective model described in section III B 1 b and the Monte Carlo algorithm, simulations were performed for $LiErF_4$ and $LiYbF_4$. Indeed, the previous version of this code has already been used to study $LiErF_4$[12] and thus try to reproduce these results with the new version is a way to test it. Furthermore, experimental data for $LiErF_4$[1] are also available for comparison. In each case, the considered system is a cubic box of $L = 7$ units cells, ie 1372 ions and $N = 10$ replicas of this box in each direction are used to compute the dipolar interactions.

a. Ordering First, it is necessary to check that the computation leads to the expected ordered state at low temperature. For $LiErF_4$ and $LiYbF_4$, without any applied external field, the antiferromagnetic order (the BLAFM structure) in the xy plane should be reached[1]. Starting from randomly oriented magnetic moments and decreasing the temperature, an ordered state is indeed obtained in each case, as shown in figure 7. The plotted parameter is the staggered magnetization in the xy plane as a function of the number of Monte Carlo steps, with a decreasing temperature in order to be sure to reach the equilibrium state at 0 K and not to stay in a configuration corresponding to a local minimum of the energy. When a small external magnetic field is applied parallel to the a-axis (respectively b-axis), the moments should align antiferromagnetically along the b-axis (respectively a-axis). The field breaks the symmetry in the xy plane and the most favourable configuration is the BLAFM structure along the axis perpendicular to the field, with the moments slightly tilted in the direction of the field. Indeed,

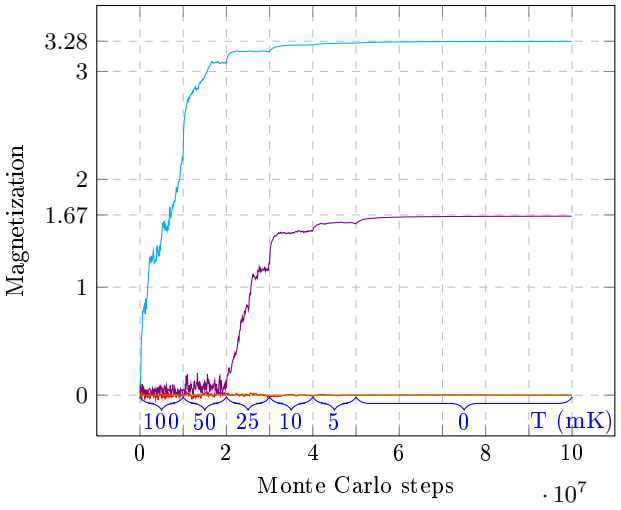

Figure 7: Apparition of the antiferromagnetic order in the xy plane in $LiErF_4$ and $LiYbF_4$. The staggered magnetization (—— for $LiErF_4$, —— for $LiYbF_4$) reaches its saturation value and the magnetization along the c-axis (—— for $LiErF_4$, —— for $LiYbF_4$) disappears.

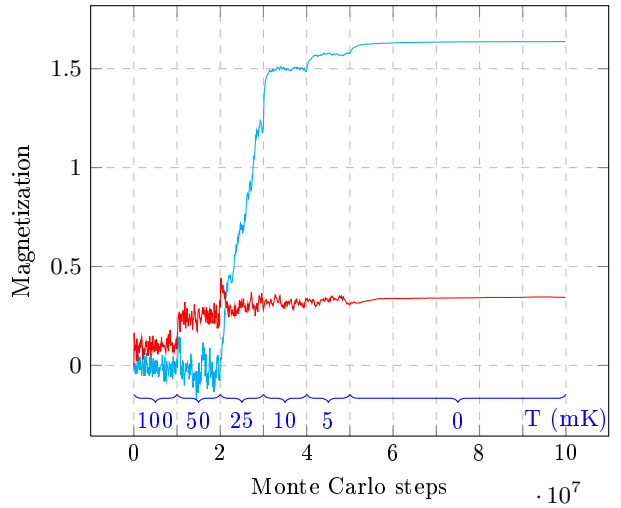

Figure 8: Apparition of the antiferromagnetic order in the xy plane in $LiErF_4$, in presence of an external field of 100 Oe parallel to the a-axis. The staggered magnetization along y —— increases until a saturation value and the moments are tilted towards the field direction (—— is the magnetization along x).

this configuration respects the interactions leading to the antiferromagnetic order and the moments can tilt in the direction of the field with a low energy cost. This effect can indeed be seen in simulations of both $LiYbF_4$ (see figure 8) and $LiErF_4$.

b. Quantum phase transition At 0 K, when an external magnetic field is applied along the c-axis, a quantum phase transition is observed. As the magnetization along z increases, the strength of the dipolar interaction decreases, which destroys the antiferromagnetic order. However, in $LiErF_4$, the simulation reveals the existence of three quantum phase transitions (see figure 9a), induced by a crossing of the energy levels of the hamiltonian $\mathcal{H}_{\rm cf} + \mathcal{H}_{\rm Z}$. The critical exponent β_H defined by:

$$J_{xy}^{\rm alt} \propto |H - H_C|^{\beta_H}$$

where $J_{xy}^{\rm alt}$ the order parameter (the staggered magnetization in the xy plane) was computed for the transition at 0.5 T. The linear fit gives $\beta_H^{\rm Er} = 0.52 \pm 0.05$. This exponent was also computed with experimental data: $\beta_H^{\rm Er} = 0.31 \pm 0.02$. The values are really different but the fit of the Monte Carlo data uses a low number of points, the result is not really accurate.
In $LiYbF_4$, a phase transition is observed in the simulation around 25 T (see figure 9b), whereas a critical field of 0.48 T was measured. This large difference is observed with the old parameters for the crystal field, which introduced an excessive anisotropy. This simulation should be carried out later with the new parameters. For $H_C = 24.75$ T, the exponent β_H was computed the same way as for $LiErF_4$. The linear fit gives $\beta_H^{\rm Yb} = 0.33 \pm 0.01$.

c. Thermal phase transition To study the thermal phase transition, temperature scans were simulated with the Monte Carlo code for both $LiErF_4$ and $LiYbF_4$. The energy per ion $\mathcal{E}$, the magnetizations J_x, J_y, J_z, the order parameter $J_{xy}^{\rm alt}$, the specific heat (from the fluctuation-dissipation theorem $C_{\rm fdt}$ and from the energy variation C_v) and the susceptibility χ were measured for each temperature using the following definitions:

$$C_{\rm fdt}(T) = \frac{\langle \mathcal{E}^2 \rangle - \langle \mathcal{E} \rangle^2}{k_B T^2}$$

$$C_v(T) = \frac{\mathcal{E}(T + {\rm d}T) - \mathcal{E}(T)}{{\rm dT}}$$

$$\chi^{\mu\nu} = \frac{1}{N_{\rm ions}\ T} \sum_{a,b} \langle J_a^\mu J_b^\nu \rangle$$

The theoretical values of the critical exponents for several universality classes are given in table II, for later comparison with the present results.

$LiErF_4$

For $LiErF_4$, the values are averaged over 109 calculations and on all the following curves, the error bars are the standard deviation of the values.
Energy per ion: To estimate the critical temperature T_N, the standard deviation of the energy per ion can be used. Indeed, at the transition the fluctuations increase, inducing a higher standard deviation of the energy values (see figure 10). The maximum of the standard deviation gives $T_N = 127$ mK. The value is lower than the experimental value (373 mK) but closer than the mean field value of 735 mK. One notices also a difference with the previous version of the code, which gave $T_N = 500$ mK.

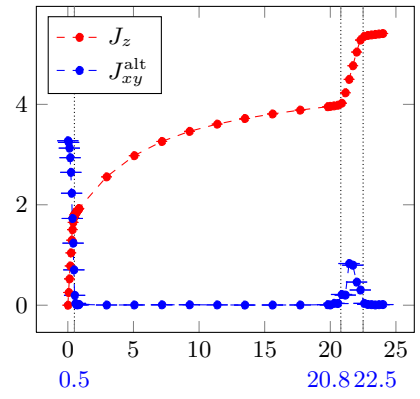

(a) $LiErF_4$

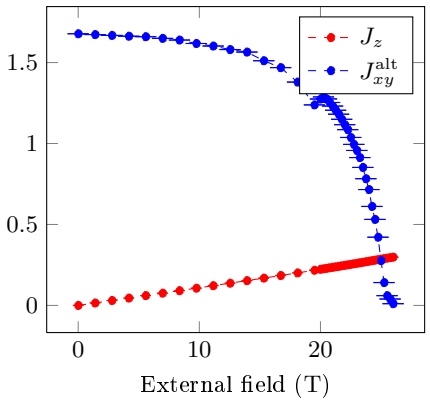

(b) $LiYbF_4$

Figure 9: Simulated field scans on $LiErF_4$ and $LiYbF_4$, at 0 K. The field is applied parallel to the c-axis. The values are averaged over 93 measurements for $LiErF_4$ and 58 measurements for $LiYbF_4$ and the errors bars are the standard deviation. Three quantum phase transitions are observed in $LiErF_4$, at 0.5 T, 20.8 T and 22.5 T. In $LiYbF_4$, a quantum phase transition is observed around 25 T, with the old parameters.

Order parameter: In both $LiErF_4$ and $LiYbF_4$, the order parameter is the staggered magnetization in the xy plane. This order parameter J_{xy}^{alt} is plotted for $LiErF_4$ in figure 11. It is more difficult here to estimate T_N. With $T_N = 124.8$ mK, the exponent β_T defined by:

$$J_{xy}^{\text{alt}} \propto |T - T_N|^{\beta_T}, \tag{14}$$

has the value $\beta_T = 0.15 \pm 0.02$ which corresponds to the experimental value of 0.15 and to the XY/h4 universality class (see table II).

Specific heat: The specific heat was computed in 2 different ways, with the fluctuation-dissipation theorem and as the derivative of the energy with respect to the temperature. The critical exponent α is defined by:

$$C \propto |T - T_N|^{-\alpha}. \tag{15}$$

Table II: Values for the critical exponents, for mean-field, 3D models[13], 2D models[14,15] and from experiment on $LiErF_4$[16].

Exponent		α	β	γ
Mean-field		0	0.5	1
3D	Ising	-0.11	0.32	1.24
	XY	0.01	0.35	1.32
	Heisenberg	0.12	0.36	1.39
2D	Ising	0	0.125	1.75
	XY/h4		0.1-0.25	
	$LiErF_4$ (at T_N)	0.28 ± 0.04	0.15 ± 0.02	0.82 ± 0.04
	$LiErF_4$ (at H_c)		0.31 ± 0.02	1.44 ± 0.2

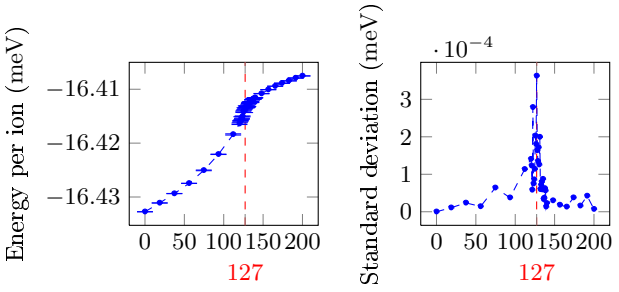

(a) (b)

Figure 10: Energy per ion and its standard deviation in $LiErF_4$. The maximum of the standard deviation gives $T_N = 127$ mK.

The exponent α was computed from both C_{fdt} for $T < T_N$ and $T > T_N$. The following values are obtained for α:

$$\begin{aligned} \alpha^{\text{fdt}}_{T<T_N} &= 0.33 \pm 0.16 \\ \alpha^{\text{fdt}}_{T>T_N} &= 0.39 \pm 0.08 \\ \alpha_{T<T_N} &= 0.27 \pm 0.21 \\ \alpha_{T>T_N} &= 0.41 \pm 0.39 \end{aligned}$$

This can be compared to the experimental value $\alpha = 0.28 \pm 0.04$. The data are noisier for $T > T_N$ because the phase is disordered, which could explain why the values measured in the ordered phase are closer to the experimental values.

Susceptibility: The magnetic susceptibility was also measured during the simulated temperature scans. The critical exponent γ is defined by:

$$\chi \propto |T - T_N|^{-\gamma}. \tag{16}$$

It was computed with a linear fit and with $T_N = 126.4$ mK, the value for γ (when $T < T_N$) is $\gamma = 0.91 \pm 0.2$.

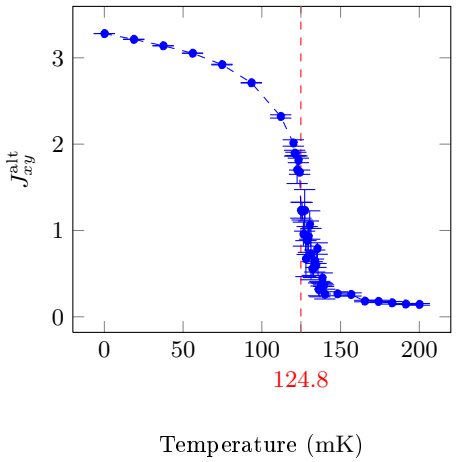

Figure 11: Order parameter in $LiErF_4$. The fluctuations around the transition make difficult to estimate precisely the critical temperature.

Table III: Values of the critical exponents for $LiErF_4$when the value of T_N (in mK) used for the fit varies. The values in blue correspond to the value of T_N given by the considered quantity.

T_N	α^{fdt}		α		β^T	γ
	$T < T_N$	$T > T_N$	$T < T_N$	$T > T_N$	$T < T_N$	$T < T_N$
122.4	**0.33**	**0.39**	0.30	0.60	0.12	0.79
123.2	0.37	0.38	0.20	0.56	0.13	0.81
124	0.35	0.39	**0.27**	**0.41**	0.14	0.82
124.8	0.32	0.39	0.37	0.50	**0.15**	0.85
125.6	0.31	0.37	0.24	0.41	0.18	0.88
126.4	0.32	0.38	0.30	0.34	0.20	**0.91**
127.2	0.29	0.34	0.32	0.14	0.23	0.94

Exponents: The values of all the mentioned exponents depend on the value of T_N used for the fit. The exponents for different T_N are given in table III.

$LiYbF_4$

For $LiYbF_4$, the values are averaged over 81 calculations. Again, the crystal field parameters are the first ones, which do not give a satisfying result for the quantum phase transition. This simulation should be performed again with the new parameters.

Energy per ion: The energy per ion and its standard deviation as a function of the temperature are plotted in figure 12. The maximum of the standard deviation gives $T_N = 34$ mK. The value is again lower than the experimental value (128 mK) and this time the mean field value is closer with 168 mK.

Order parameter: The order parameter J_{xy}^{alt} in $LiYbF_4$ is plotted in figure 13. Again, T_N is not easy to estimate. With $T_N = 34.4$ mK, the fit gives $\beta_T = 0.18 \pm 0.01$, which is again in the range of exponents for the XY/h4 class.

Specific heat: As in $LiErF_4$, the specific heat was

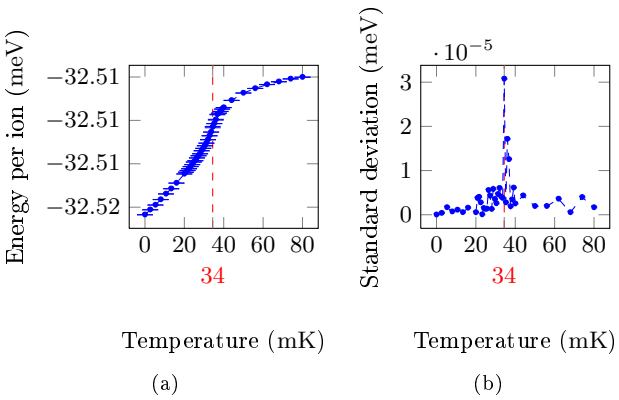

Figure 12: Energy per ion and its standard deviation in $LiYbF_4$. The maximum of the standard deviation gives $T_N = 34$ mK.

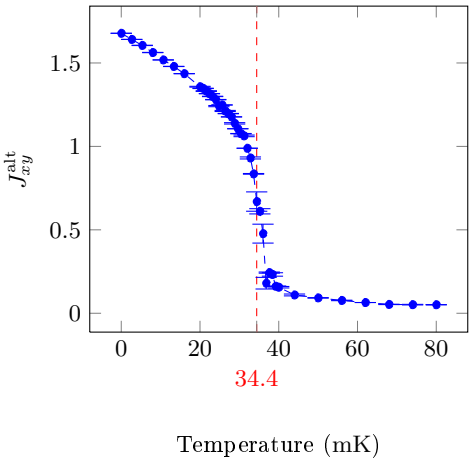

Figure 13: Order parameter in $LiYbF_4$. The critical temperature is difficult to find, but between 33 mK and 37 mK.

computed with the fluctuation-dissipation theorem and as the derivative of the energy with respect to the temperature. The exponent α was also computed in both case for $T < T_N$ and $T > T_N$. The following values are obtained for α:

$$\alpha^{\text{fdt}}_{T<T_N} = 0.25 \pm 0.07$$
$$\alpha^{\text{fdt}}_{T>T_N} = 0.59 \pm 0.14$$
$$\alpha_{T<T_N} = 0.28 \pm 0.08$$
$$\alpha_{T>T_N} = 0.53 \pm 0.18$$

As for $LiErF_4$, the data are noisier in the disordered phase, which can explain the difference between both phases.

Susceptibility: The magnetic susceptibility in $LiYbF_4$as a function of the temperature was also measured. γ was

Table IV: Dependence on T_N (in mK) of the exponents in $LiYbF_4$, the blue values correspond to the value of T_N given by the considered quantity.

T_N	α^{fdt}		α		β^T	γ
	$T < T_N$	$T > T_N$	$T < T_N$	$T > T_N$	$T < T_N$	$T < T_N$
33.6	0.20	0.68	**0.28**	0.75	0.16	0.89
34.4	0.24	0.66	0.33	0.73	**0.18**	**0.90**
35.2	**0.25**	**0.59**	0.32	0.67	0.23	0.98
36	0.29	0.56	0.34	**0.53**	0.26	1.01

Table V: Comparison of the critical exponents for $LiErF_4$ and $LiYbF_4$ in the ordered phase. The values are close and correspond to the experimental values in $LiErF_4$. The values for β_T correspond to the

	α^{fdt}	α	β_T	γ
$LiErF_4$(MC)	0.33	0.27	0.15	0.91
$LiErF_4$(exp)	0.28		0.15	
$LiYbF_4$(MC)	0.25	0.28	0.18	0.90

computed using a linear fit and with $T_N = 34.4$ mK, the value when $T < T_N$ is $\gamma = 0.90 \pm 0.2$.

Exponents: As in $LiErF_4$, the values of the exponents depend on the value of T_N. This dependence is shown in table IV.

Comparison

The critical exponents in $LiErF_4$ and $LiYbF_4$ are compared in table V. When the exponents are computed in the ordered phase, all the values are close and correspond to the experimental values for $LiErF_4$. Hence $LiYbF_4$ and $LiErF_4$ show similar critical behaviors, which agree with the 2D XY universality class.

IV. SQUID MEASUREMENTS

A. Estimation of the composition of samples of $LiHo_{1-x}Er_xF_4$

The Monte Carlo simulation described in section III B could also be used to study $LiHo_{1-x}Er_xF_4$ or $LiHo_{1-x}Yb_xF_4$. In these compounds, the disorder must be taken into account and at low temperature, a spin glass phase appears. An experimental study of $LiHo_{1-x}Er_xF_4$ has already been done[17] and a phase diagram T_C-x is known[3]. However, the values of x were known with an accuracy of 5% and hence a method to measure x more accurately was needed. Here, a method to find x in $LiHo_{1-x}Er_xF_4$ using measurements of magnetic moments in a Superconducting Quantum Interferometric Device (SQUID) is detailed.

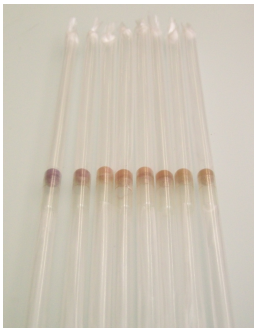

Figure 14: Picture of the 8 samples of $LiHo_{1-x}Er_xF_4$ prepared, from the $LiErF_4$ on the left to the $LiHoF_4$ on the right.

1. *Principle of the SQUID measurement*

A SQUID is an instrument used to measure magnetic moments and whose opering principle is based on a useful property of superconducting rings which is that the magnetic flux inside them is quantized[17]. A SQUID is constituted of a superconducting ring which is interrupted by one or two Josephson junctions. A Josephson junction is a thin layer of insulator between two superconductors and through which the Cooper pairs can pass via quantum tunneling. With two Josephson junctions and when a bias current is applied across the ring, the magnetic flux generates an oscillating voltage, with one oscillation for each flux quantum passing through the ring. This allows accurate measurements of the magnetic moment of a sample which is passed through the superconducting ring.

2. *Preparation of the samples*

In order to measure the magnetic moment of the samples as accurately as possible, the demagnetization effect must be taken into account (see Appendix C). Since the only shape allowing a uniform magnetization when a uniform magnetic field is applied on a sample is the ellipsoid, it was necessary to prepare spherical powder samples. They were prepared in plastic capsules, and the powder was mixed with an epoxy encapsulant called Stycast to avoid that the particles in the powder align in the magnetic field. The samples of $LiHo_{1-x}Er_xF_4$ are shown on the figure 14.

3. *Estimation of the reproducibility*

Five samples of $C_{15}H_{21}Fe\,O_6$ with Stycast were prepared to check the reproducibility of the preparation and two field scans preceded by a degaussing procedure were performed on each sample. The degaussing procedure is used to remove a potential remnant field in the magnet. One observes that the addition of Stycast allows to get

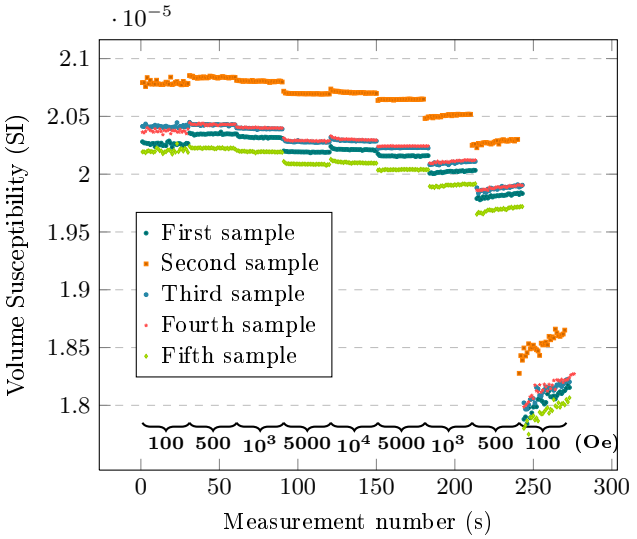

Figure 15: Field scans of 5 different sample of $C_{15}H_{21}Fe\,O_6$ with Stycast, at $T = 30$ K. During each scan, the field is swept from 10^2 Oe to 10^4 Oe and then decreased again to 10^2 Oe.

exactly the same values for each scan on a given sample, excepted for the low field of 10^2 Oe where the signal is noisier. Furthermore, the signal has exactly the same shape for all the samples and the differences between the values may be due to the variations in the mass of powder (see figure 15). 5 samples were prepared, with 2 field scans for each, with 9 values for the field (the decreasing and increasing field are separated, they do not give the same values of susceptibility) and 30 points for each field in each scan. With these data, several reproducibility criteria can be defined:

- the reproducibility of the measurement on a given sample, at a given field, during a given scan.
- the reproducibility of a full field scan on a sample.
- the reproducibility of the sample preparation, ie of the mass of powder which constitutes the sample.
- the variation of the susceptibility value with the field.

a. Reproducibility of the measurement with all the conditions fixed. For each sample, during each field scan, the moment of the sample was measured 30 times for each field value. The standard deviation for these 30 values was computed in each case, and averaged over the 10 scans. The variation is very low, below 0.1%: in given conditions the measurement is very reproducible.

b. Reproducibility of a full field scan on a sample. Two similar field scans were performed on each sample, with a degaussing procedure before each. The mean differences between both scans were calculated and finally, with the degaussing procedure, the two field scans are rather similar, the difference is 1.5 % in the worst case.

Table VI: Evaluation of the different reproducibility criteria with the 5 spheres of $C_{15}H_{21}Fe\,O_6$.

Error on the measurement with the conditions fixed	between 0.02 and 0.09 %
Variation between 2 scans on the same sample	between 0.2 and 1.5 %
Error on the mass of the sample	around 1%
Variation of the susceptibility value with the field	around 3.5%

c. Reproducibility of the sample preparation. The main source of error in the preparation of the samples is the mass of the powder which is used. The standard deviation between the 10 scans of the values for each field was computed and averaged over the 30 measurements. The error due to the sample preparation is around 1%. It could be reduced by weighting the powder with more accuracy.

d. Variation of the susceptibility with the field. The variation of the value of the susceptibility when the value of the field changes (for instance because of demagnetization) can also be evaluated, which leads to evaluate the standard deviation of the whole measurement for each scan on each sample. 10 values are obtained and averaged. The final value is a variation of 3.4 %. However, since the temperature scans on the $LiHo_{1-x}Er_xF_4$ samples are done at a fixed field, it is not necessary to consider this error in the following measurements.
Finally, the estimation of the errors coming from the 4 criteria are gathered in table VI.

4. *Measurements on* $LiHo_{1-x}Er_xF_4$.

Eight samples of $LiHo_{1-x}Er_xF_4$ were then prepared, with the following compositions: $LiHoF_4$, 2 samples to compare the results, 80% of Ho, 55% of Ho, 50% of Ho, 30% of Ho, 25% of Ho, $LiErF_4$. A temperature scan from 10 K to 300 K was performed on each sample with a field of 10^4 Oe, to avoid the noise at low field. One observes that the two samples of $LiHoF_4$ give almost exactly the same result.
The effect of demagnetization on the sample must be taken into account (see Appendix C). Assuming that the samples are spherical, the volume magnetization can be written:

$$M = \chi\,(H_0 - \frac{M}{3}) \tag{17}$$

where H_0 is the external magnetic field and χ the volume susceptibility. The susceptibility follows the Curie law at high temperatures:

$$\chi = \frac{C}{T} \tag{18}$$

In this temperature range, the interactions are not considered and then C should be linear in the fraction of Ho,

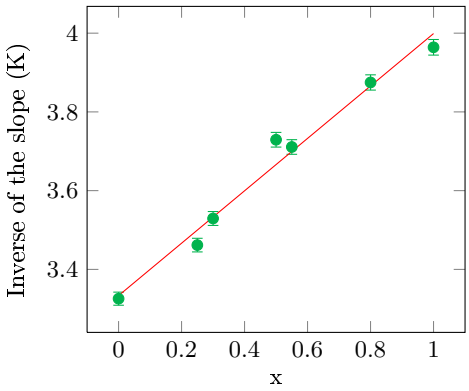

Figure 16: x dependence of the inverse of the slopes of H_0/M and linear fit.

Table VII: Comparison between the computed values of the fractions of Ho and the expected ones.

Expected fraction of Ho	Computed fraction of Ho
1	0.95
0.80	0.81
0.55	0.57
0.50	0.59
0.30	0.29
0.25	0.19
0	-0.01

x. Hence:

$$\frac{M}{H_0} = \frac{3C}{C+3T}. \tag{19}$$

The relationship between H_0/M and T should be linear with a slope of $1/C$, which leads to the fact that the inverse of the slopes should be linear in x, at least at high temperatures. The values of the inverse of the slopes as a function of x are plotted on the figure 16, with an error bar of 1% corresponding to the reproducibility of the preparation of the spheres. Using this linear fit, it is possible to compute the fraction of Ho in each sample and to compare it with the expected value (see table VII). The data show a rather good agreement but the difference is still high for some samples. This technique to measure x could be improved by measuring more accurately the mass of the samples. Furthermore, since Ho and Er both have a large magnetic moment with similar values — the variation in the slope is rather small and it is difficult to distinguish the samples. Therefore, using this method on $LiHo_{1-x}Yb_xF_4$ should be easier because the magnetic moment of Yb is really smaller than the one of Ho, leading to a larger variation of the slopes and then to an improved accuracy.

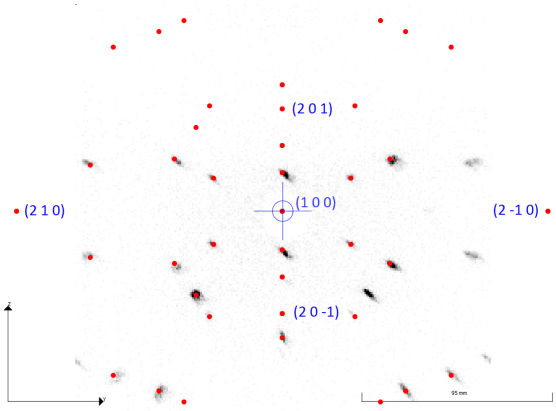

Figure 17: Observed diffraction pattern along the a-axis in $LiYbF_4$. The red dots are the expected theoretical pattern, some points are missing because of a defect with the software used.

B. Measurements of a cube of $LiYbF_4$

1. *Preparation of the sample*

A measurement of the magnetic moment of a single crystal of $LiYbF_4$ was performed in a SQUID. A cubic sample was used to take into account more easily the demagnetization factor. Because of the anisotropy of the material, it was necessary to align the sample before cutting it, in order to measure the components χ_a and χ_c of the susceptibility tensor. This alignment was performed using Laue diffraction. The theoretical diffraction pattern and the observed one are shown in figure 17.

2. *Temperature scans*

a. Anisotropy and powder averaging The cube was measured twice in the SQUID, two temperature scans were performed between 2.5 K and 300 K, one with the external field parallel to the a-axis and the other with the field parallel to the c-axis. The applied DC field was 500 Oe in both cases. The powder sample was measured in the 100 K to 300 K temperature range. The anisotropy between the a-axis and the c-axis can be found from the values of the susceptibility which is much larger along the a-axis than along the c-axis (figure 18). For a powder sample, the susceptibility corresponds to an average between the susceptibility along each axis:

$$\chi_{\text{powder}} = \frac{2}{3}\chi_a + \frac{1}{3}\chi_c \tag{20}$$

Figure 18 shows a very good agreement between the average value of the data measured on the single crystal and on the powder sample.

b. Fit with a Curie-Weiss law and comparison with mean field calculation The dependence of the molar sus-

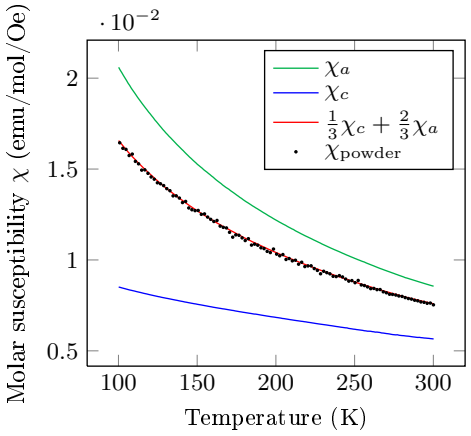

Figure 18: Temperature scans with an external field of 500 Oe on the single crystal and the powder sample, compared with the average of χ_a and χ_c.

ceptibility with the temperature can be expressed (in a mean field approximation) with a Curie-Weiss law:

$$\chi = \frac{g_L^2 \mu_B^2 J(J+1)}{3k_B(T-\theta)} \mathcal{N}_A \tag{21}$$

where $\mathcal{N}_A$ is the Avogadro number. This leads to the definition of an effective moment $\mu_{\text{eff}} = g_L\sqrt{J(J+1)}\mu_B$. The susceptibilities along the a-axis and the c-axis were computed in two different ways: with the mean field approximation and with the fluctuation dissipation theorem, using the formula 22 for the susceptibility.

$$\chi^{\mu\nu}_{\text{FDT}} = \frac{\mu_B^2 g_L^2}{k_B T} \left(\langle J^\mu J^\nu \rangle - \langle J^\mu \rangle \langle J^\nu \rangle \right) \tag{22}$$

where

$$\langle A \rangle = \frac{\sum_\lambda e^{-\beta E_\lambda} \langle \lambda | A | \lambda \rangle}{\sum_\lambda e^{-\beta E_\lambda}}$$

(with $\{\lambda\}$ the set of eigenvalues of $\mathcal{H}_{\text{cf}} + \mathcal{H}_{\text{Z}}$ and $\beta = 1/k_B T$). A Curie-Weiss law was fitted to both the experimental and numerical data, to obtain the values of μ_{eff}. This was also done with data on powder samples of $LiErF_4$ and $LiHoF_4$. The results are presented in table VIII and a comparison between the mean field computation, the results of the fluctuation-dissipation theorem and the experimental data is shown in figure 19 for $LiYbF_4$. The values of μ_{eff} obtained with the different methods are in good agreement and the differences comes from the fact that the mean field approximation takes the dipolar interaction into account whereas the fluctuation-dissipation does not. Furthermore, the theoretical values of μ_{eff} do not consider the crystal field levels, which explains that they do not really correspond to the experimental value.
In $LiYbF_4$, a change in slope in $1/\chi$ is found at around

Table VIII: Effective moments from the Curie-Weiss law for the experimental data, the mean field calculation and the fluctuation-dissipation theorem. The effective moments are given in μ_B.

		μ_{eff} exp.	μ_{eff} MF	μ_{eff} FDT	μ_{eff} th.[10]
$LiYbF_4$	aa	4.85	4.58	4.76	
	cc	5.20	5.68	4.06	
	average	4.75	4.68	4.53	4.5
	powder	4.74			4.5
$LiHoF_4$	powder	10.45	10.66	10.60	10.6
$LiErF_4$	powder	9.53	9.71	9.58	9.6

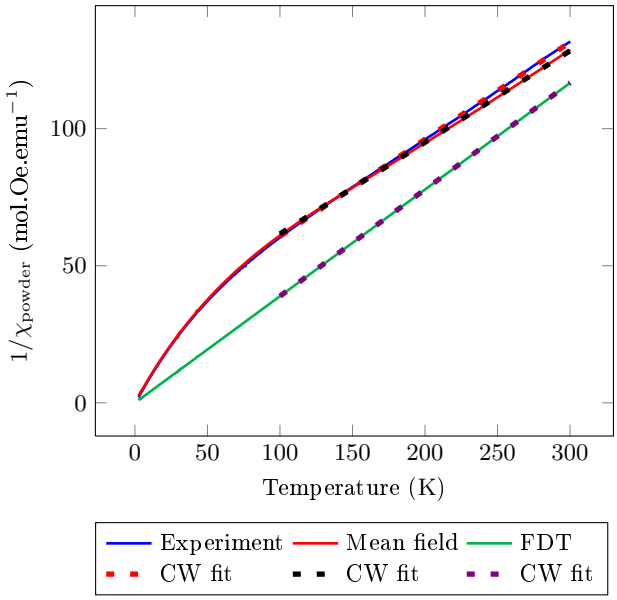

Figure 19: Curves of the inverse susceptibility for $LiYbF_4$, comparison with the mean field approximation and the fluctuation-dissipation theorem and Curie-Weiss fits of the data at high temperature.

50 K. This change does not occur either in $LiErF_4$ or in $LiYbF_4$. A plausible explanation could be that at this temperature, a new energy level of the crystal field becomes populated, however, further experimental measurements are required to understand this. Furthermore, this change does not appear in the fluctuation-dissipation theorem calculation but does in the mean field one, which suggests that it could be linked to the interactions or to some collective phenomena.

V. THE H-T PHASE DIAGRAM OF $LiYbF_4$

A. Experimental setup

1. *AC susceptibility measurements*

To study the low temperature behavior of $LiYbF_4$, AC susceptibility measurements were performed on a single

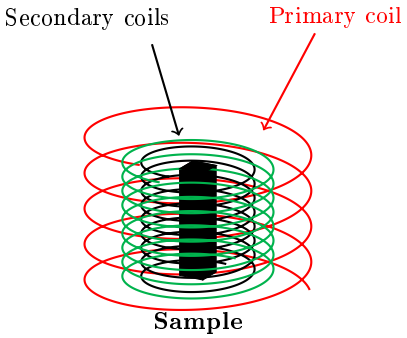

Figure 20: Schema of the inductive susceptometer.

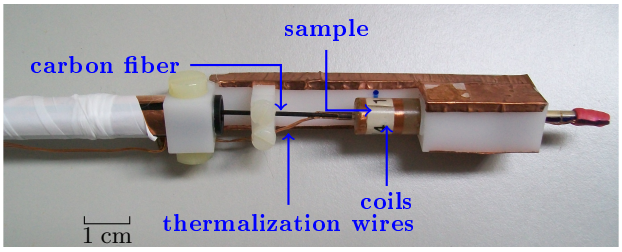

Figure 21: Picture of the susceptometer used in the dilution refrigerator to map out the phase diagram of $LiYbF_4$.

crystal in a dilution refrigerator. The AC susceptibility χ_{AC} is defined by:

$$\chi_{AC} = \frac{\mathrm{d}M}{\mathrm{d}H} \tag{23}$$

where M is the magnetization of the sample and H an external low AC magnetic field. More precisely[18], if an alternating magnetic field $H_a = H_{a0}\cos(\omega t)$ is applied to the sample, the real part χ' and the imaginary part χ'' of the AC susceptibility are defined by:

$$\chi' = \frac{\omega}{\mu_0 H_{a0}\pi}\int_0^{\frac{2\pi}{\omega}} \langle B\rangle \cos(\omega t)\mathrm{d}t \ - 1$$

$$\chi'' = \frac{\omega}{\mu_0 H_{a0}\pi}\int_0^{\frac{2\pi}{\omega}} \langle B\rangle \sin(\omega t)\mathrm{d}t$$

where $\langle B\rangle$ is the local average flux density in the sample. The technique used here for the measurements is the inductive technique. The sample is located inside three concentric coils (see figure 20): a primary coil and two compensated secondary coil. The primary coil produces the AC field and the two secondary coils (pickup coils) are used to measure the response of the sample. These coils are wrapped with opposite polarity, in order to reduce the voltage induced by the AC field. The signal is measured with a lock-in amplifier in order to observe only the component which is at the frequency of the AC field (here 546.5 Hz).The measured signal is then proportional to the susceptibility and to the frequency of the AC field:

$$v_{rms} \propto f H_{a0}\chi$$

where f and H_{a0} are the frequency and the amplitude of the applied AC magnetic field. The real part χ' of the susceptibility is the slope of the $M(H)$ curve and the imaginary part χ'' is related to dissipation processes.

2. *The dilution refrigerator*

The critical temperature in $LiYbF_4$ is predicted to be 185 mK by the mean field calculation. In order to measure it experimentally, the sample is cooled down to a very low temperature. Using liquid ^{4}He, it is possible to reach 4.2 K and when the vapour pressure is reduced, temperatures around 1 K are reachable. For lower temperatures, one can use a dilution refrigerator. In a dilution refrigerator, a mixture of liquid ^{3}He and ^{4}He is used. Below a critical temperature, a phase separation occurs. The lighter phase is rich in ^{3}He and thus called the concentrated phase, and the heavier phase (the dilute phase) is rich in ^{4}He. The enthalpy of ^{3}He in the two phases is different and therefore evaporating ^{3}He from the concentrated to the dilute phase provides cooling. This process works even at very low temperature because the concentration of ^{3}He in the dilute phase is non zero at 0 K. Figure 22 shows a photo of the dilution refrigerator. The mixture is condensed in the 1 K pot. It flows to the mixing chamber, where the phase boundary is located, through the heat exchanger. The ^{3}He is then evaporated in the dilute phase, passes again through the heat exchanger and is pumped from the still before being returned to the 1 K pot. During the operation, the refrigerator is placed inside a cryostat which is cooled down to 4.2 K using liquid ^{4}He.
At the low temperatures which are reached by the dilution refrigerator, the measurement of the temperature is performed using a ruthenium oxide resistor which is calibrated according to the method described in Appendix D. This type of resistors are not affected significantly by small magnetic fields and can be used down to around 15 mK. Below this temperature, the resistance becomes almost constant, which leads to rather inaccurate measurements.

3. *Preparation of the sample*

The measurements were performed on a single crystal of $LiYbF_4$, of approximately 1×1×10 mm. The crystal was aligned using Laue diffraction (see figure 17). Both the external DC field (applied with a 18 T superconducting magnet) and the AC field were parallel to the c-axis of the crystalline structure, allowing the measure of χ_{cc}. Four thin copper wires were fixed on the sample to ensure a good thermalization. A stick of carbon fiber was also

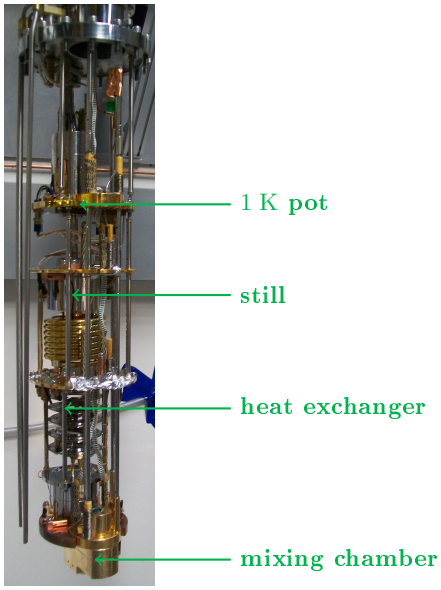

Figure 22: Picture of the dilution refrigerator. The susceptometer is fixed at the bottom of the mixing chamber during the measurement.

attached on the sample to facilitate its manipulation.

B. Results

1. *Critical temperature*

In order to map out the H-T phase diagram of $LiYbF_4$, temperature and field scans were performed on the sample. To determine the critical temperature, the complex susceptibility was measured without any external DC field between the base temperature of the refrigerator and 250 mK. The real part χ' shows a peak (see figure 23) at the phase transition with $T_c = 128.6$ mK. This value can be compared to the result of the mean field computation, which gives $T_c^{\mathrm{MF}} = 186$ mK when the hyperfine coupling is not considered and $T_c^{\mathrm{MF}} = 182$ mK when it is taken into account. As expected, the mean field overestimates the critical temperature because it neglects the fluctuations. Conversely, the Monte Carlo simulation underestimates the critical temperature, $T_c^{\mathrm{MC}} = 34.4 \pm 3$ mK but this value was computed with the wrong parameters.

2. *Critical field*

The critical field H_C was found from performing a field scan at the base temperature of the refrigerator, 14.3 mK. The curves of χ' and χ'' are plotted in figure 24. The response of the sample looks different when the field is increased or decreased. This effect could be due to a too high ramp rate during the scans, which introduces eddy

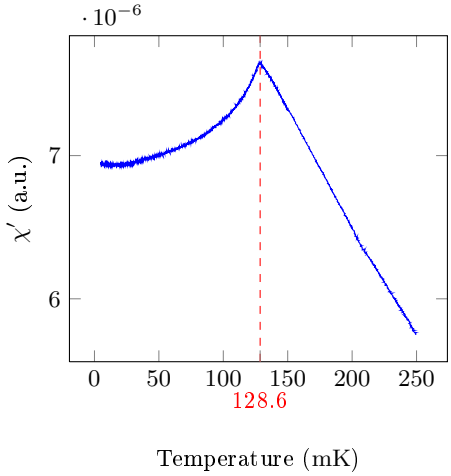

Figure 23: Real part χ' of the AC susceptibility as a function of the temperature in $LiYbF_4$, without external magnetic field. The measured critical temperature is $T_c = 128.6$ mK

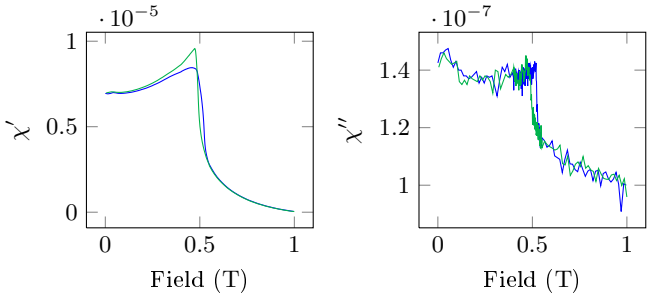

Figure 24: Field scan at 14.3 mK. The scan was performed twice, once with the field going up —— and the other one with the field going down ——. The ramp rate is 0.04 T/min, excepted between 0.4 and 0.55 T where it is reduced to 4 mT/min

currents heating the sample space. Several scans with different ramp rates were carried out to check this hypothesis (see Appendix E) and indeed, when the ramp rate is decreased, the two curves become closer but even at the slowest possible ramp rate, they do not overlap perfectly. Another explanation is that the thermalization of the sample is really difficult to achieve because at low temperature, the thermal conductivity becomes very small. Thus the temperature might be different between the two scans and inhomogeneous in the sample, leading to this hysteretic behaviour.

3. *Phase diagram*

Several field scans at different temperatures were then carried out on the sample with a ramp rate of 0.8 mT/min. In each case, the position of the peak in

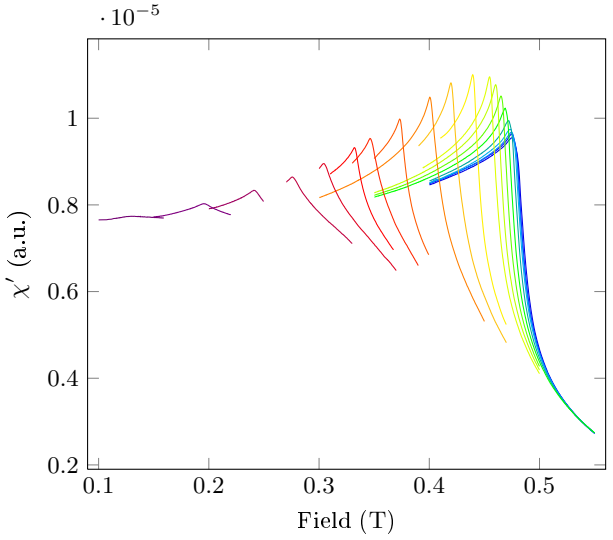

Figure 25: χ' when the external DC field varies, for different temperatures between 14.3 mK and 120 mK. The critical field decreases when the temperature increases and the amplitude of the peak decreases at very low temperature.

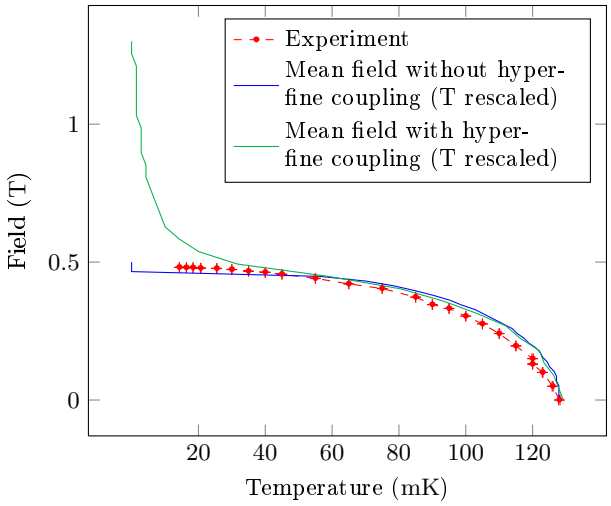

Figure 26: H-T phase diagram of $LiYbF_4$.

the susceptibility indicates the transition: each scans gives one point for the phase diagram. All these field scans are plotted in figure 25. As expected, the critical field decreases when the temperature increases. Furthermore, the amplitude of the peak does not vary monotonically with the temperature. At high temperature, the amplitude is low (and the peak disappears when $T > T_N = 128$ mK), when the temperature decreases, the amplitude of the peak increases until a maximum around 50 mK. Then, at lower temperatures, the amplitude of the peak decreases. In fact, the peak becomes also less sharp below 30 mK. This low temperature effect was also observed in $LiErF_4$ and could be due to the hyperfine coupling.

At low fields, some temperature scans were also performed to study the behaviour of the sample around T_N. Finally, the phase diagram of the figure 26 was obtained from analysing (at low temperatures) the χ'' part of the susceptibility which showed the onset of the phase transition more clearly than χ'. These data can be compared to the results given by the mean field calculation. The calculation in the mean field approximation was done with and without the hyperfine coupling and the values for T_N and H_C are given in table IX. With the hyperfine coupling, at very low temperature, the critical field is increased. This effect was seen in $LiErF_4$ but here with $LiYbF_4$, it seems that below 20 mK, the sample was not well thermalized. The temperature may have stayed around 20 mK and since the change of slope in the phase diagram occurs below 20 mK, the effect would not have been visible.
Two critical exponents can be defined on the phase diagram, to describe the behaviour of $T_N(H)$ when $H \to H_C$ and the behaviour of $H_C(T)$ when $T \to T_N$. They were

Table IX: Values for T_N and H_C given by the mean field approximation.

Experiment	$T_N = 128.6$ mK $H_C = 0.48$ T
MF without hyperfine coupling	$T_N = 186$ mK $H_C = 0.46$ T
MF with hyperfine coupling	$T_N = 182$ mK $H_C = 1.2$ T

computed for both the experimental data and the numerical ones coming from mean field (with and without hyperfine coupling). For $T_N(H)$, the experiment gives an exponent of 0.32 ± 0.02 while the mean field gives 0.24 ± 0.01. The experimental value of this exponent in $LiErF_4$[1] is 0.34 ± 0.01, which is close to the value measured in $LiYbF_4$. Again, the two compounds seem to have the same behaviour. For $H_C(T)$, the experimental value of the exponent is 0.54 ± 0.05, whereas the mean field gives 0.52 ± 0.03 without the hyperfine interaction and 0.50 ± 0.04 with them. In this case, the mean field approximation gives a rather good description of the behaviour of $LiYbF_4$.

VI. DISCUSSION

When the first set of crystal field is used, a large discrepancy between the results of the numerical simulations on $LiYbF_4$ and the experimental data is observed. The critical temperature in $LiYbF_4$ is very underestimated by the Monte Carlo computation and both the mean field calculation and the Monte Carlo give a critical field which is 50 times the one which was measured. Furthermore, the change in slope around 50 K in the susceptibility curve 19 cannot be explained from the values of the transitions between energy levels in the crystal

field. All these observations suggest that these crystal field parameters for $LiYbF_4$ might be wrong.
However, transitions between the levels in the used $\mathcal{H}_{\rm cf}$ correspond to those measured with neutron scattering. There might be another transition at a lower energy which was not seen but from the data that can be found in the literature[19], it seems rather implausible. In addition, the change of slope in the susceptibility was present in the mean field data, which were computed with these crystal field parameters.
A new fit of the neutron scattering data, using also the measurement of susceptibility of the single crystal performed in the SQUID, was done in order to find a new set of parameters. The mean field calculations using these new parameters (table X) give a critical field which corresponds to the experiment. The Monte Carlo simulation should be carried out again with these parameters but should give a more reasonable value for H_C since the anisotropy in the xy plane is less pronounced.
Nevertheless, even with the wrong parameters, the obtained values of the critical exponents are in agreement. The Monte Carlo simulation gives for α, β and γ similar values for $LiYbF_4$ and $LiErF_4$, and these values also correspond to those obtained from experiments for $LiErF_4$. Furthermore, the exponent measured on the phase diagrams for $T_N(H)$ are really close: 0.32 for $LiYbF_4$ and 0.34 for $LiErF_4$. Both compounds seem to have similar low temperature behaviours.

Acknowledgments

I would like to thank Henrik Rønnow, the head of the laboratory, for having offered to me the opportunity of doing my internship in the LQM and for the useful discussions he had with me. I also thank Peter Babkevich, Julian Piatek, Bastien Dalla Piazza and Ivan Kovacevic who worked with me for their valuable help and advice and for their cheerfulness. I am grateful to all the members of the LQM for their friendliness. Finally, I am also thankful to Caroline Pletscher who helped me with the administrative tasks.

Appendix A: Stevens operators and crystal field parameters

The charge distribution around each rare earth ion creates an electric field (the crystal field) acting on the $4f$ electrons and creating the magnetic anisotropy. The contribution of the crystal field to the potential energy is written:

$$\mathcal{V}_{\rm cf}(\vec{r}) = \int \frac{e\rho(\vec{R})}{|\vec{r}-\vec{R}|}{\rm d}\vec{R}$$

where $\rho(\vec{R})$ is the charge density. After a development in spherical harmonics and some manipulation[10], the crystal field can be written in terms of the Stevens operators:

$$\mathcal{H}_{\rm cf} = \sum_i \sum_{lm} B_l^m \hat{O}_l^m(\vec{J}_i)$$

Table X: Crystal field parameters, in meV. For $LiYbF_4$, the first set of parameters was used in the Monte Carlo simulation but was not satisfying. The second one (which is inside the intervals given by the error bars of the first) was obtained from fitting the neutron scattering data and the susceptibility data and were used for the other calculations.

	$LiYbF_4$[20]	$LiYbF_4$ (new)	$LiErF_4$[1]	$LiHoF_4$[6]
$10^3 B_2^0$	663 ± 80	646.2	60.23	-60.0
$10^3 B_4^0$	12.5 ± 4.5	15.3	-0.12	0.350
$10^3 B_4^4(c)$	102 ± 41	116.5	-4.33	3.60
$10^5 B_6^0$	-62 ± 73	-68.6	-0.19	4.0
$10^3 B_6^4(c)$	-16.0 ± 1.7	-15.2	-0.085	0.070
$10^6 B_6^4(s)$	0	0	-22.7	9.8

In the case of $LiREF_4$, the symmetries of the crystalline structure lead to a reduction of the number of parameters. The expression of the relevant operators are the following: (where $X \equiv J(J+1)$ and $\hat{J}_\pm \equiv \hat{J}_x \pm i\hat{J}_y$)

$$\begin{aligned}
\hat{O}_2^0 &= 3\hat{J}_z^2 - X \\
\hat{O}_4^0 &= 35\hat{J}_z^4 - (30X-25)\hat{J}_z^2 + (3X^2-6X) \\
\hat{O}_4^4 &= \frac{1}{2}(\hat{J}_+^4 + \hat{J}_-^4) \\
\hat{O}_6^0 &= 231\hat{J}_z^6 - (315X-735)\hat{J}_z^4 \\
&\quad + (105X^5 - 525X + 294)\hat{J}_z^2 \\
&\quad + (-5X^3 + 40X^2 - 60X) \\
\hat{O}_6^4(c) &= \frac{1}{4}[(11\hat{J}_z^2 - X - 38)(\hat{J}_+^4 + \hat{J}_-^4) \\
&\quad + (\hat{J}_+^4 + \hat{J}_-^4)(11\hat{J}_z^2 - X - 38)] \\
\hat{O}_6^4(s) &= \frac{1}{4i}[(11\hat{J}_z^2 - X - 38)(\hat{J}_+^4 - \hat{J}_-^4) \\
&\quad + (\hat{J}_+^4 - \hat{J}_-^4)(11\hat{J}_z^2 - X - 38)]
\end{aligned}$$

Appendix B: Equilibrium configuration for the Monte Carlo simulation

In both $LiYbF_4$ and $LiErF_4$, there are two types of phase transitions : the classical thermal phase transition and a quantum phase transition, at 0 K, which occurs when an external magnetic field is applied perpendicularly to the xy plane. Using the Monte-Carlo code, field scans and temperature scans can be performed but before studying the transitions, an estimation of the number of Monte Carlo steps needed to reach equilibrium is required. The scans are carried out in the following way:

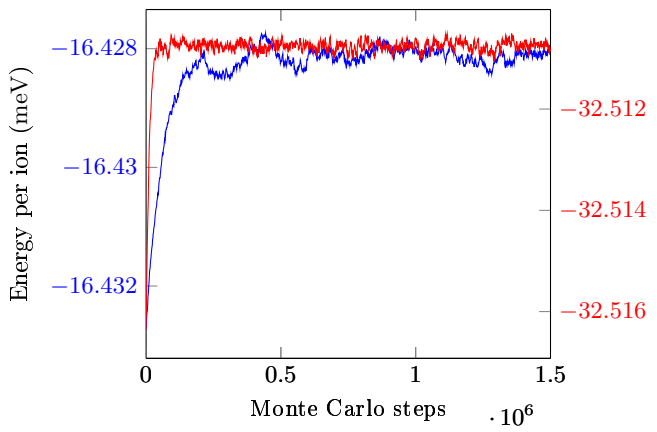

Figure 27: Energy relaxation for $LiErF_4$ —— and $LiYbF_4$ ——, for a system of size $L = 7$ and a temperature step of 50 mK.

the system is set in the equilibrium configuration for the considered temperature and field using N_{eq} Monte Carlo steps. The directions of the moments after this procedure are saved and used to measure the parameters of interest during N_{meas} iterations. Several independent measurement can be executed in the same equilibrium configuration. In order to estimate the value of N_{eq}, which depends on the size of the system (here L is kept at 7 in all the following, thus this effect was not taken into account), on the size of the temperature or field step and of the nature of the ion, Er or Yb. Figure 27 shows the initial configuration of the system which is the BLAFM structure at 0 K and the temperature is set to 50 mK, which represents a higher step than what is used during the scans, whose temperature steps are smaller than 20 mK. For $LiErF_4$, the relaxation after the temperature change takes approximately 10^6 steps, whereas for $LiYbF_4$ only $2 \cdot 10^5$ steps are required, for the same temperature variation of 50 mK. For a field variation of 1 T, the energy relaxation lasts $1.5 \cdot 10^6$ steps in $LiErF_4$ but is really longer in $LiYbF_4$, around $6 \cdot 10^6$ steps are needed. However, $2 \cdot 10^6$ steps seem sufficient to approach the equilibrium. Some measurements were performed with $N_{\text{eq}} = 10^7$ and $N_{\text{meas}} = 3 \cdot 10^6$ in order to check that the relaxation was long enough. They gave the same results as those with the smaller N_{eq} and N_{meas}. Finally, the values $N_{\text{eq}} = 2 \cdot 10^6$ and $N_{\text{meas}} = 10^6$ are used in the following, for both $LiErF_4$ and $LiYbF_4$.

Appendix C: Demagnetization factor

In order to express the magnetization of a sample, two magnetic fields should be taken into account: the applied external field $\vec{H}_0$ and the *demagnetizing field* $\vec{H}_d$. This field is induced by the magnetization of the sample itself and is opposed to the external field. Thus, the relation between the magnetization and the field is:

$$\vec{M} = \chi(\vec{H}_0 + \vec{H}_d)$$

The value of $\vec{H}_d$ depends on the geometry of the sample and most of the time, it is not uniform. In a uniform external field $\vec{H}_0$, the only shape of the sample leading to a uniform magnetization is the ellipsoid[21]. In this case, the demagnetizing field is linearly related to the magnetization:

$$\vec{H}_d = -\mathcal{N}\vec{M}$$

where $\mathcal{N}$ is the *demagnetization factor*, which is a diagonal tensor in the basis of the principal axes of the ellipsoid. This tensor has two general properties: it is symmetric and its trace is 1. Hence, for a sphere, because of the spherical symmetry, $\mathcal{N}_{xx} = \mathcal{N}_{yy} = \mathcal{N}_{zz} = \frac{1}{3}$. For non-ellipsoidal bodies, the demagnetization factor in not uniform inside the sample. In order to evaluate the average response of the sample, an averaging procedure is needed. There are two main methods used to obtain an averaged demagnetization factor. In the first one, the factor is averaged over the whole body and is called the demagnetization factor. For the second method, the average is only taken on a section of the sample which is perpendicular to the applied field and the factor is called the ballistic demagnetization factor. For a cube, along the principal axes, the magnetometric demagnetization factor is then the same as for the sphere, $\mathcal{N}_{xx} = \mathcal{N}_{yy} = \mathcal{N}_{zz} = \frac{1}{3}$.

Appendix D: Calibration of the thermometers

In order to measure accurately the temperature of the sample in the dilution refrigerator, a thermometer made of a thick film of ruthenium oxide is used. This thermometer allows to measure temperatures down to 15 mK. The calibration of the thermometer is performed using a superconducting reference device (SRD) and a paramagnetic salt called CMN (cerium magnesium nitrate). The SRD contains 13 superconducting samples with known and sharp transitions at temperatures between 14 mK and 7 K. The paramagnetic susceptibility of the CMN is measured simultaneously and then fitted to a Curie-Weiss law:

$$\chi = \frac{C}{T - \theta_{\text{CW}}}$$

using the 13 known temperatures from the SRD. Using this fit, the thermometer can be calibrated over the entire temperature range. In addition, before the thermometer can be used to measure accurately the temperature, it must be thermally cycled. This procedure consists of cooling the thermometer down to 77 K one hundred times using liquid nitrogen. This cycling is required to reduce the variability of the resistance.

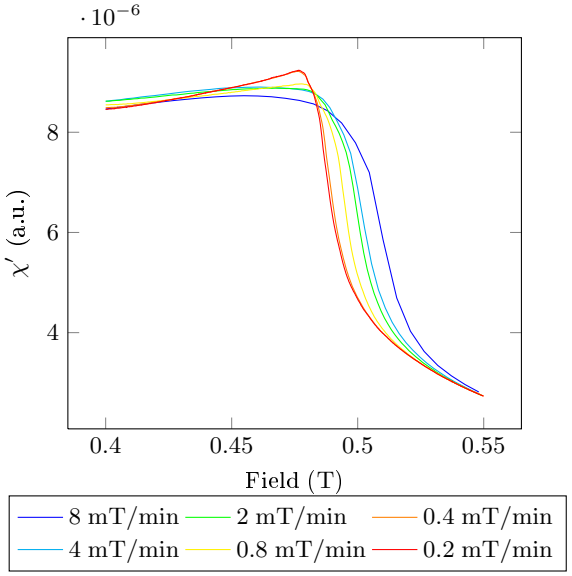

Figure 28: Field scans between 0.4 and 0.55 T at 14.3 mK for different ramp rates. The peak in χ' becomes sharper when the rate decreases.

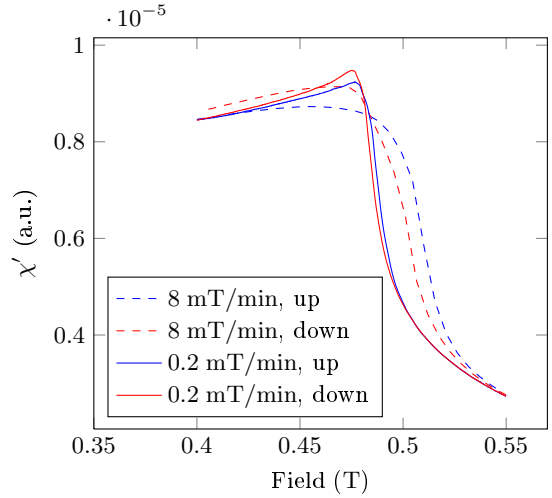

Figure 29: Field scans at 14.3 mK for the maximum and the minimum ramp rates used. The hysteretic behavior is still visible at the lowest rate, but the difference becomes smaller.

Appendix E: Effect of the ramp rate on the field scans in $LiYbF_4$

At very low temperature, the shape of the peak in χ' for a field scan changes and is amplitude decreases. It becomes less sharp and therefore the transition is difficult to find accurately. One has to use the peak in χ'' instead. An explanation for the shape of the peak in χ' could be that the field was increased too fast. Several scans at different rates were performed to look at this effect (figure 28). Indeed, the shape of the curve changes when the rate changes, probably because the time of thermalization is longer at low temperature since the thermal conductivity is very small. However, even at the slowest possible ramp rate, there is still a difference between the scans with the field going up and down (see figure 29).

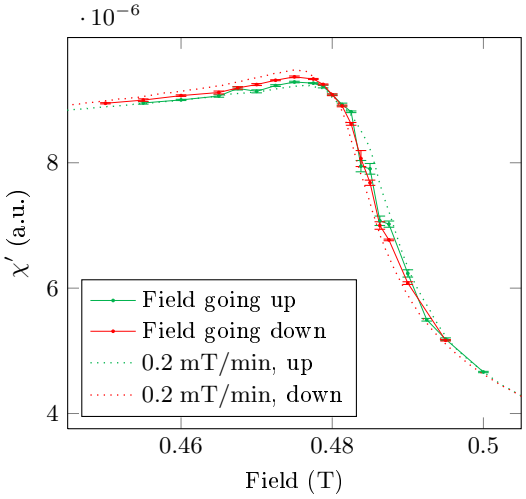

Figure 30: Comparison between the slowest field scans and the points taken with the relaxation of one hour, at 14.3 mK. The value here is the mean value of χ' over the last 30 min and the error bar gives the variation during this period of time.

Since the lowest possible ramp rate of the magnet (0.2 mT/min) was reached, another method was used. The field was set to a given value and then the relaxation was measured during one hour. 15 values of the magnetic field were taken, with the field going up and the field going down. The result of this measurement is plotted in figure 30. The obtained points are as expected between the two curves from the slowest field scans. This time, the curves for the increasing and decreasing field are really close.

[1] C. Kraemer, N. Nikseresht, J. O. Piatek, N. Tsyrulin, B. Dalla Piazza, K. Kiefer, B. Klemke, T. F. Rosenbaum, G. Aeppli, C. Gannarelli, et al., Science **336**, 1416 (2012).

[2] J. Luttinger and L. Tisza, Physical Review **70**, 954 (1946).

[3] J. O. Piatek, B. Dalla Piazza, N. Nikseresht, N. Tsyrulin, I. Živković, K. W. Krämer, M. Laver, K. Prokes, S. Mataš,

N. B. Christensen, et al., Phys. Rev. B **88**, 014408 (2013).
[4] International Union of Crystallography, *International Tables for Crystallography*, vol. A (2006).
[5] S. K. Misra and J. Felsteiner, Physical Review B **15**, 4309 (1977).
[6] H. Rønnow, J. Jensen, R. Parthasarathy, G. Aeppli, T. Rosenbaum, D. McMorrow, and C. Kraemer, Physical Review B **75**, 054426 (2007).
[7] R. Chui, R. Orbach, and B. L. Gehman, Phys. Rev. B **2**, 2298 (1970).
[8] R. W. Berends and L. Maleki, J. Opt. Soc. Am. B **9**, 332 (1992).
[9] D. Brewer, *Progress in Low Temperature Physics*, vol. VII B (North Holland, 1978).
[10] J. Jensen and A. R. Mackintosh, *Rare earth magnetism* (Clarendon Oxford, 1991).
[11] G. Marsaglia, The Annals of Mathematical Statistics **43**, 645 (1972).
[12] G. Klughertz, Master's thesis, EPFL (2012).
[13] P. M. Chaikin and T. C. Lubensky, *Principles of condensed matter physics*, vol. 1 (Cambridge Univ Press, 2000).
[14] F. Kagawa, K. Miyagawa, and K. Kanoda, Nature **436**, 534 (2005).
[15] A. Taroni, S. T. Bramwell, and P. C. Holdsworth, Journal of Physics: Condensed Matter **20**, 275233 (2008).
[16] N. N. Ghanepour, Ph.D. thesis, EPFL (2012).
[17] J. Piatek, Ph.D. thesis, EPFL (2012).
[18] M. Nikolo, American Journal of Physics **63**, 57 (1995).
[19] H. Dong, W. Zheng, and S. Wu, physica status solidi (b) **240**, 120 (2003).
[20] C. Kraemer, Ph.D. thesis, ETH-Zurich (2009).
[21] J. Maxwell, *A treatise on electricity and magnetism*, vol. 2 (Oxford: Clarendon, 1873).